High-Field EPR Study of Resonance-Delocalized $[Fe_2(OH)_3(tmtacn)_2]^{2+}$

Michael J. Knapp,[†] J. Krzystek,[‡] Louis-Claude Brunel,[‡] and David N. Hendrickson*,[†]

Department of Chemistry and Biochemistry-0358, University of California at San Diego, La Jolla, California 92093, and the Center for Interdisciplinary Magnetic Resonance, National High Magnetic Field Laboratory, Tallahassee, Florida 32310

Received January 21, 1999

High-frequency EPR data are reported for the Fe(II/III) valence delocalized dinuclear complex $[Fe_2(OH)_3(tmtacn)_2]^{2+}$. A full-matrix diagonalization approach is used to derive the spin-Hamiltonian parameters for this $S_T = {}^9/_2$ complex. At high fields (up to 14.5 T) and high frequencies (189−433 GHz) fine structure peaks due to resonances between the Kramers doublets ($M_s = {}^9/_2, {}^7/_2, ...$) are observed. The spacing of the fine structure reveals that the axial zero-field splitting (ZFS) parameter D is $+1.08(1)$ cm^{-1}; a very small rhombic ZFS ($|E| \leq 0.01$ cm^{-1}) is suggested by line broadening of these interdoublet resonances. Simulations reveal that **g** is close to 2.00, and very nearly isotropic: $g_x = g_y = g_z = 2.00(2)$. This complex is a model for the valence-delocalized $[Fe_2S_2]^+$ pairs found in larger iron−sulfur clusters, such as the cofactors from the nitrogenase system. This work indicates that HFEPR is a viable technique for the study of high-spin centers in proteins.

Introduction

Polynuclear iron complexes play an important role in many biological processes. The largest is found in ferritin,[1] an iron storage protein that contains ca. 4500 Fe atoms and is absolutely essential for Fe homeostasis. Smaller complexes are found in the nitrogenase enzymes,[2] in which complexes ranging from the exotic "FeMoco," $[Fe_7MoS_9]$, which is the site of dinitrogen reduction, to the "P clusters", $[Fe_8S_{7-8}]$, and the more fundamental $[Fe_4S_4]$ clusters, are to be found. Protein sites with two non-heme iron atoms are numerous, and fall into one of two large classes: dinuclear iron−sulfur sites, in which the two Fe atoms are bridged by two sulfide bridges; and dinuclear iron-oxo sites, in which the two Fe atoms are bridged by oxo/hydroxo and carboxylato bridges. The iron−sulfur sites function almost exclusively as electron-transfer cofactors,[3] while the iron-oxo proteins have diverse functions, from O_2 storage in hemerythrin[3] to O_2 activation in methane monooxygensase.[4] Both of these two types of proteins exhibit $S = {}^1/_2$ ground states that are distinguishable by X-band EPR, for $[Fe_2S_2]^+$ sites exhibit[5] $g_{av} = 1.94$, and $[Fe_2(\mu\text{-OH})(\mu\text{-COO})_2]^{2+}$ sites typically[4] exhibit $g_{av} < 1.9$, which provides a spectroscopic probe as to the identity of structurally noncharacterized dinuclear Fe proteins. In all of these dinuclear Fe protein sites, chemistry is dictated by the ligand structure, which in turn is reflected by the strength of magnetic interactions between the two Fe atoms.

The study of dinuclear transition metal complexes has advanced the understanding of both bioinorganic chemistry and basic magnetism. In recent years, the interplay of resonance delocalization and isotropic magnetic exchange in these dimers has received enormous interest,[6−27] principally due to the recognition of the importance of resonance delocalization in high-spin dinuclear complexes. In particular, the theoretical and calculational work of Noodleman,[28−37] Girerd,[7,12−18,24,25] and their co-workers has demonstrated that resonance delocalization plays a dominant role in determining the electronic structure of $[Fe_2S_2]^+$ mixed-valence complexes. In such a dinuclear complex formed by high-spin metal sites, Heisenberg exchange tends to favor an antiparallel alignment of spins on the two Fe ions, stabilizing states with small total spin, while resonance delocalization favors parallel spin alignment, stabilizing states with large total spin. The exact nature of the ground state depends on the ratio between the Heisenberg exchange term $[-J(S(S +$

[†] University of California at San Diego.
[§] National High Magnetic Field Laboratory.

(1) Lippard, S. J.; Berg, J. M. *Principles of Bioinorganic Chemistry*; University Science Books: Mill Valley, CA, 1994.
(2) Howard, J. B.; Rees, D. C. *Chem. Rev.* **1996**, *96*, 2965−2982.
(3) Holm, R. H.; Kennepohl, P.; Solomon, E. I. *Chem. Rev.* **1996**, *96*, 2239−2314.
(4) Wallar, B. J.; Lipscomb, J. D. *Chem. Rev.* **1996**, *96*, 2625−2657.
(5) Hagen, W. R. In *Iron−Sulfur Proteins*; Cammack, R., Ed.; Academic Press: San Diego, 1992; Vol. 38, p 165.
(6) Crouse, B. R.; Meyer, J.; Johnson, M. K. *J. Am. Chem. Soc.* **1995**, *117*, 9612−9613.
(7) Münck, E.; Papaefthymiou, V.; Surerus, K. K.; Girerd, J. J. In *Metal Clusters in Proteins*; Que, L., Jr., Ed.; American Chemical Society: Washington, DC, 1988; pp 302−325.
(8) Noodleman, L. *Inorg. Chem.* **1991**, *30*, 246−256.
(9) Barone, V.; Bencini, A.; Ciofini, I.; Daul, C. A.; Totti, F. *J. Am. Chem. Soc.* **1988**, *110*, 8357−8365.
(10) Bertini, I.; Luchinat, C. *J. Biol. Inorg. Chem.* **1996**, *1*, 183−185.
(11) Bertrand, P.; Gayda, J. P. *Biochim. Biophys. Acta* **1979**, *579*, 107−121.
(12) Blondin, G.; Girerd, J. J. *J. Biol. Inorg. Chem.* **1996**, *1*, 170−172.
(13) Bominaar, E. L.; Borshch, S. A.; Girerd, J. J. *J. Am. Chem. Soc.* **1994**, *116*, 7957−7957.
(14) Bominaar, E. L.; Borshch, S. A.; Girerd, J. J. *J. Am. Chem. Soc.* **1994**, *116*, 5362−5372.
(15) Bominaar, E. L.; Hu, Z. G.; Münck, E.; Girerd, J. J.; Borshch, S. A. *J. Am. Chem. Soc.* **1995**, *117*, 6976−6989.
(16) Bominaar, E. L.; Achim, C.; Borshch, S. A.; Girerd, J. J.; Münck, E. *Inorg. Chem.* **1997**, *36*, 3689−3701.
(17) Borshch, S. A.; Bominaar, E. L.; Blondin, G.; Girerd, J. J. *J. Am. Chem. Soc.* **1993**, *115*, 5155−5168.
(18) Borshch, S. A.; Bominaar, E. L.; Girerd, J. J. *New J. Chem.* **1993**, *17*, 39−42.
(19) Day, E. P.; Pederson, J.; Bonvoisin, J. J.; Moura, I.; Moura, J. J. G. *J. Biol. Chem.* **1988**, *263*, 3684−3689.
(20) Ding, X. Q.; Bominaar, E. L.; Bill, E.; Winkler, H.; Trautwein, A. X.; Drueke, S.; Chaudhuri, P.; Wieghardt, K. *J. Chem. Phys.* **1990**, *92*, 178−186.
(21) Ding, X. Q.; Bominaar, E. L.; Bill, E.; Winkler, H.; Trautwein, A. X.; Drueke, S.; Chaudhuri, P. H.; Wieghardt, K. *Hyperfine Interactions* **1990**, *53*, 311−315.

10.1021/ic9901012 CCC: $18.00
Published on Web 05/29/1999

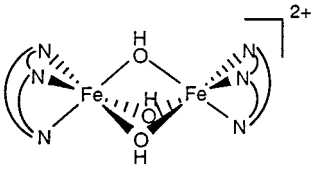

Figure 1. Schematic diagram of the $[Fe_2(\mu\text{-}OH)_3(tmtacn)_2]^{2+}$ cation.

1))] and the resonance delocalization term $[B(S + {}^1/_2)]$. It was postulated that a decrease in $|J|$, as occurs upon converting the μ_2-S^{2-} to μ_3-S^{2-} bridges, or an increase in $|B|$, could lead to a $S = {}^9/_2$ spin for a (Fe^{II}−Fe^{III}) complex. With the experimental work of Münck et al.[7] on $[Fe_3S_4]^{0+}$ clusters, it became clear that resonance delocalization was the dominant form of magnetic interaction in determining the spin-state energies of $[Fe_2]$ pairs bridged by μ_3-sulfide ions, as revealed by their valence-delocalized nature and large ground-state spin.

Weighardt and co-workers reported the properties of the $[Fe_2(OH)_3(tmtacn)_2]^{2+}$ cation (Figure 1) in 1989.[20,22] The cation has a geometry that approaches D_{3h} symmetry, with the C_3 axis along the Fe−Fe vector, indicating that this is likely the principal axis (z axis) of the electronic structure (**g** and **D** tensors). These workers determined that the $S = {}^9/_2$ ground-state results from strong resonance delocalization ($B = 1300$ cm^{-1} from absorption spectroscopy), and experiences a relatively large zero-field splitting ($D = +1.8$ cm^{-1}) and an anisotropic **g** tensor ($g_x = g_y = 2.04$, $g_z = 2.30$) as given by the spin Hamiltonian:

$$H = \mathbf{g}\beta\mathbf{SH} + D(\mathbf{S}_z^2 - {}^1/_3S(S+1)) \qquad (1)$$

These results were obtained by an analysis of the Mössbauer and X-band EPR spectra. More recently, the $[Fe_2(OH)_3(tmtacn)_2]^{2+}$ complex was studied in detail by Solomon and co-workers[23,24] to determine the pathway for resonance delocalization and to characterize the excited electronic states. It was shown that the principal delocalization pathway was a direct Fe−Fe σ bonding interaction facilitated by the short Fe−Fe distance (2.51 Å). Magnetic susceptibility data were used to derive the spin Hamiltonian parameters $g_{av} = 2.1$ and $D = 2.28$ cm^{-1}, which are in good agreement with those obtained by Wieghardt et al.[20,22] The $S = {}^9/_2$ state was shown to result from a combination of large resonance delocalization and a small Heisenberg exchange ($|J| < 70$ cm^{-1}).

Many bio-clusters, such as the P clusters and the FeMoco of nitrogenase, are characterized by large spin states and large zero-field splittings (ZFS),[38,39] with the result being that conventional EPR techniques only permit indirect information on the magnitude of the zero-field splittings and **g** tensors. High-frequency (>100 GHz) electron paramagnetic resonance (HFEPR) has been used very recently to study molecules with large ground-state spins.[40−53] Many of these studies involved oriented polycrystalline samples, where the large magnetic fields employed oriented the crystallites. This field-induced orientation of crystallites is only possible when the crystals have an easy axis of magnetization, such as arises for molecules with $D < 0$ that are nearly aligned in the crystal. There have been very few HFEPR studies on powdered samples,[42,44,47,48,50] and only four HFEPR studies[42,47,54,55] on systems with $D > 0$. HFEPR has proven very useful for determining electronic fine structure, such as zero-field splittings, that are too large for effective study at conventional EPR frequencies (e.g., X-band at 9 GHz). The HFEPR technique uses relatively high-energy radiation (ca 3−15 cm^{-1}), and this leads to the direct observation of resonances between Kramers or non-Kramers doublets for even large values of D. As a consequence, the ZFS parameters can be determined with much greater precision than is possible with variable-temperature X-band EPR on Kramers systems. It also makes non-Kramers systems accessible. In addition, by performing HFEPR at several different frequencies, the resonance positions

(22) Drueke, S.; Chaudhuri, P.; Pohl, K.; Wieghardt, K.; Ding, X.-Q.; Bill, E.; Sawaryn, A.; Trautwein, A. X.; Winkler, H.; Gurman, S. J. *J. Chem. Soc., Chem. Commun.* **1989**, 59.
(23) Gamelin, D. R.; Bominaar, E. L.; Kirk, M. L.; Wieghardt, K.; Solomon, E. I. *J. Am. Chem. Soc.* **1996**, *118*, 8085−8097.
(24) Gamelin, D. R.; Bominaar, E. L.; Mathoniere, C.; Kirk, M. L.; Wieghardt, K.; Girerd, J. J.; Solomon, E. I. *Inorg. Chem.* **1996**, *35*, 4323−4335.
(25) Girerd, J. J. *J. Chem. Phys.* **1983**, *79*, 1766−1775.
(26) Krockel, M.; Grodzicki, M.; Papaefthymiou, V.; Trautwein, A. X.; Kostikas, A. *J. Biol. Inorg. Chem.* **1996**, *1*, 173−176.
(27) Mohanta, S.; Nag, K.; Dutta, S. K.; Werner, R.; Haase, W.; Duin, E.; Johnson, M. K. *Ber. Bunsen-Ges. Phys. Chem. Chem.* **1996**, *100*, 2086−2090.
(28) Noodleman, L.; Case, D. A.; Sontum, S. F. *J. Chim. Phys. Phys.-Chim. Biol.* **1989**, *86*, 743−755.
(29) Jordanov, J.; Roth, E. K. H.; Fries, P. H.; Noodleman, L. *Inorg. Chem.* **1990**, *29*, 4288−4292.
(30) Noodleman, L. *Inorg. Chem.* **1991**, *30*, 256−264.
(31) Noodleman, L.; Case, D. A. In *Advances in Inorganic Chemistry*; Cammack, R., Ed.; Academic Press: New York, 1992; Vol. 38, pp 423−470.
(32) Mouesca, J. M.; Chen, J. L.; Noodleman, L.; Bashford, D.; Case, D. A. *J. Am. Chem. Soc.* **1994**, *116*, 11898−11914.
(33) Mouesca, J. M.; Noodleman, L.; Case, D. A. *Inorg. Chem.* **1994**, *33*, 4819−4830.
(34) Mouesca, J. M.; Noodleman, L.; Case, D. A. *Int. J. Quantum. Chem.* **1995**, 95−102.
(35) Noodleman, L.; Peng, C. Y.; Case, D. A.; Mouesca, J. M. *Coord. Chem. Rev.* **1995**, *144*, 199−244.
(36) Mouesca, J. M.; Noodleman, L.; Case, D. A.; Lamotte, B. *Inorg. Chem.* **1995**, *34*, 4347−4359.
(37) Noodleman, L.; Case, D. A.; Mouesca, J. M.; Lamotte, B. *J. Biol. Inorg. Chem.* **1996**, *1*, 177−182.
(38) Lindahl, P. A.; Day, E. P.; Kent, T. A.; Orme-Johnson, W. H.; Münck, E. *J. Biol. Chem.* **1985**, *260*, 11160.
(39) Surerus, K. K.; Hendrich, M. P.; Christie, P. D.; Rottgardt, D.; Orme-Johnson, W. H.; Münck, E. *J. Am. Chem. Soc.* **1992**, *114*, 8579−8590.
(40) Aubin, S. M. J.; Dilley, N. R.; Pardi, L.; Krzystek, J.; Wemple, M. W.; Brunel, L. C.; Maple, M. B.; Christou, G.; Hendrickson, D. N. *J. Am. Chem. Soc.* **1998**, *120*, 4991−5004.
(41) Goldberg, D. P.; Telser, J.; Krzystek, J.; Montalban, A. G.; Brunel, L. C.; Barrett, A. G. M.; Hoffman, B. M. *J. Am. Chem. Soc.* **1997**, *119*, 8722−8723.
(42) Dei, A.; Gatteschi, D.; Pardi, L.; Barra, A. L.; Brunel, L. C. *Chem. Phys. Lett.* **1990**, *175*, 589−592.
(43) Barra, A. L.; Caneschi, A.; Gatteschi, D.; Sessoli, R. *J. Magn. Magn. Mater.* **1998**, *177*, 709−710.
(44) Barra, A. L.; Gatteschi, D.; Sessoli, R.; Abbati, G. L.; Cornia, A.; Fabretti, A. C.; Uytterhoeven, M. G. *Angew. Chem., Int. Ed. Engl.* **1997**, *36*, 2329−2331.
(45) Barra, A. L.; Gatteschi, D.; Sessoli, R. *Phys. Rev. B−Condensed Matter* **1997**, *56*, 8192−8198.
(46) Barra, A. L.; Debrunner, P.; Gatteschi, D.; Schulz, C. E.; Sessoli, R. *Europhys. Lett.* **1996**, *35*, 133−138.
(47) Rentschler, E.; Gatteschi, D.; Cornia, A.; Fabretti, A. C.; Barra, A. L.; Shchegolikhina, O. I.; Zhdanov, A. A. *Inorg. Chem.* **1996**, *35*, 4427−4431.
(48) Barra, A. L.; Caneschi, A.; Gatteschi, D.; Sessoli, R. *J. Am. Chem. Soc.* **1995**, *117*, 8855−8856.
(49) Barra, A. L.; Brunel, L.-C.; Gatteschi, D.; Pardi, L.; Sessoli, R. *Acc. Chem. Res.*. **1998**, *31*, 460−466.
(50) Telser, J.; Pardi, L.; Krzystek, J.; Brunel, L. C. *Inorg. Chem.* **1998**, in press.
(51) Brunel L. C.; Barra, A. L.; Martinez, G. *Physica B* **1995**, *204*, 298−302.
(52) Caneschi, A.; Gatteschi, D.; Sessoli, R.; Barra, A. L.; Brunel, L. C.; Guillot, M. *J. Am. Chem. Soc.* **1991**, *113*, 5873−5874.
(53) Barra, A. L.; Brunel, L. C.; Robert, J. B. *Chem. Phys. Lett.* **1990**, *165*, 107−109.
(54) Champion, P. M.; Sievers, A. J. *J. Chem. Phys.* **1977**, *66*, 1819−1825.
(55) Alpert, Y.; Couder, Y.; Tuchendler, J.; Thome, H. *Biochim. Biophys. Acta* **1973**, *322*, 34−37.

may be tracked in order to determine the principal components of the **g** tensor. This can lead to a considerably improved understanding of the electronic structure and reactivity of biologically relevant Fe complexes.

The $[Fe_2(OH)_3(tmtacn)_2]^{2+}$ complex is a suitable test complex to check the utility of HFEPR to the study biological Fe complexes exhibiting appreciable resonance exchange. This complex is relatively unique in that it is one of only two[27] dinuclear Fe complexes that are both high-spin and valence-delocalized; therefore, it is more amenable to detailed studies than the protein-bound, $S = {}^9/_2$ $[Fe_2S_2]^+$ systems recently studied by Johnson et al.[6,56] The $[Fe_4S_4]^{2+}$ small molecule systems,[7,15,35,37] while exhibiting resonance delocalization within each $[Fe_2S_2]^+$ dimer, are diamagnetic due to inter-pair magnetic exchange and hence are EPR silent. The model complex $[Fe_2(OH)_3(tmtacn)_2]^{2+}$ was chosen for study by HFEPR not only to characterize its ground-state properties, but also to illustrate the utility of HFEPR to study high-spin sites in proteins.

Experimental Section

The compound $[Fe_2(OH)_3(tmtacn)_2][ClO_4]_2 \cdot 2MeOH \cdot 2H_2O$ (**1**) was prepared by published methods[22] using commercially available reagents.

High-frequency EPR experiments were performed at the National High-Magnetic Field Laboratory in Tallahasee, Florida. A superconducting Oxford magnet system (14.5 T) capable of high sweep rates (0.5 T/min) was used. The large field sweeps that were performed (0−14 T) required relatively rapid field-sweep rates (0.5 T/min). This introduced a small field hysteresis as measured by the magnet power supply current, as described elsewhere.[50] The hysteresis was accounted for by running a spectrum at a given frequency in both field-sweep directions, and taking the resonant field position as the average of the two scans. The microwave sources were two Gunn diodes of 95 and 110 GHz nominal frequency. Harmonic generators permitted experiments at frequencies of $n \times 95$ and $n \times 110$ GHz, where n is an integer between 1 and roughly 4 as the power falls off rapidly at the higher harmonics. High-pass filters were used to cut out lower harmonics; however, higher harmonics frequently were evident in the experimental spectra. A helium-cooled bolometer was used as the detector. Further details will be described in a forthcoming paper.[57]

The experiments described in this report were performed using a single-pass transmission setup. This configuration is characterized by a lower sensitivity than the one using a resonator in terms of absolute number of spins/gauss detectable. However, due to much larger sample volume (up to 0.5 mL) available in the transmission configuration, and the fact that at high frequencies only multi-mode resonators of relatively low conversion factors can be used, the difference in sensitivity between the two versions is lower than one might expect, approximately 1 order of magnitude.[57] The single-pass setup has the great advantage of operation over a broad range of frequencies. As will follow from the article, this multifrequency capability is of great help in identifying and following EPR transitions in the complicated spectra that characterize high-spin states.

EPR spectra were simulated using the computer program SIM.[58−60] SIM calculates the energy levels of the spin state by full-matrix diagonalization of the spin Hamiltonian. The standard spin Hamiltonian was used (eq 1), in which it was assumed that **D** and **g** are collinear. The derivation of the matrix elements used for this study is given in the Supporting Information. Resonant fields were determined by the energy differences between levels, with the simulated line shape determined by considering both transition probabilities and Boltzmann population differences between the energy levels. The output from SIM was used to construct the angular dependence plots.

Results and Discussion

HFEPR Measurements. Magnetic susceptibility measurements[23] have established that the ground state of $[Fe_2(OH)_3(tmtacn)_2](ClO_4)_2 \cdot 2MeOH \cdot 2H_2O$ (complex **1**) is $S = {}^9/_2$. This ground-state results because resonance delocalization ($B = 1300$ cm^{-1}) dominates the weak Heisenberg exchange interaction ($|J| < 70$ cm^{-1}). The energy expression for the pure spin states in this complex is shown below (eq 2).

$$E_S = -JS(S+1) \pm B(S+{}^1/_2) \qquad (2)$$

The $S = {}^9/_2$ state is well isolated, for the nearest excited spin state is estimated[23] to lie at least 700 cm^{-1} higher in energy. The only populated energy levels at low temperatures will be the M_s levels that derive from the $S = {}^9/_2$ ground state. Mössbauer experiments[20,22] have established that the two iron sites are equivalent, indicating that the $(Fe^{2+}-Fe^{3+})$ formal valences are actually delocalized, such that the cation in complex **1** is best described as $(Fe^{2.5+})_2$. The ZFS was shown to be dominantly axial, and was estimated to be $D = +1.8$ or $+2.3$ cm^{-1} by the above-mentioned Mössbauer and magnetic studies, respectively. X-band EPR experiments[20] revealed broad resonances at $g' = 10.2$ and $g' \cong 2.3$ characteristic of the lowest-lying $\pm{}^1/_2$ Kramers doublet of the $S = {}^9/_2$ ground state, suggesting that **g** is anisotropic ($g_\perp = 2.04$, $g_{//} = 2.3$).

The above evaluations of ZFS by both Mössbauer and magnetic susceptibility data rely upon the thermal population of the various M_s levels, and their responses to a magnetic field. These techniques provide reasonable estimates for D but lack the precision available from EPR spectroscopy, in which the transitions $M_s \rightarrow (M_s + 1)$ are directly observed. D is much larger (ca. 1 cm^{-1}) than the microwave energy at X-band frequencies (ca. 0.3 cm^{-1}), and therefore the only resonances observed in X-band EPR experiments are those between the $\pm{}^1/_2$ Kramers doublet which provide no information on the magnitude of the ZFS **D** parameter. Furthermore, the X-band EPR resonances are very broad, which lead to uncertainty in evaluating g values.

HFEPR spectra were collected over the 189−430 GHz frequency range at 20 K on a finely ground sample of complex **1** pressed into a KBr pellet. The obvious advantage of HFEPR over X-band EPR spectroscopy is that more transitions are observed, as shown in Figure 2. A series of regularly spaced lines which results from ZFS of the $S = {}^9/_2$ ground state, called fine structure, is observed due to transitions between the M_s and $(M_s + 1)$ levels.

The spin-Hamiltonian[61] that describes the $S = {}^9/_2$ ground state of the $[Fe_2(OH)_3(tmtacn)_2]^{2+}$ cation is shown below (eq 3),

$$H = \mathbf{g}\beta\mathbf{SH} + D[\mathbf{S}_z^2 - {}^1/_3S(S+1)] + E[\mathbf{S}_x^2 - \mathbf{S}_y^2] \qquad (3)$$

where the zero-field splitting of the ground state is represented by the last two terms, where D is the axial zero-field splitting and E gauges the rhombic ZFS; higher-order ZFS terms have been neglected. The symmetry of the $[Fe_2(OH)_3(tmtacn)_2]^{2+}$ cation approaches D_{3h}, and a strictly axial ZFS is called for in this symmetry since $[\mathbf{S}_x^2 - \mathbf{S}_y^2] = 0$. However, a small rhombic ZFS may be observed, since the cation does not occupy a site of rigorous D_{3h} symmetry in the crystal.[22,23] For this reason,

(56) Johnson, M. K.; Duin, E. C.; Crouse, B. R.; Golinelli, M. P.; Meyer, J. in *Spectroscopic Methods in Bioinorganic Chemistry*; Solomon, E. I., Hodgson, K. O., Eds.; American Chemistry Society: Washington, DC, 1998; Vol. 692, pp 286−301.
(57) Hassan, A.; Pardi, L. A.; Krzystek, J.; Sienkiewicz, A.; Rohrer, M.; Brunel, L. C. Manuscript in preparation.
(58) Jacobsen, C. J. H.; Pedersen, E.; Villadsen, J.; Weihe, H. *Inorg. Chem.* **1993**, *32*, 1216−1221.
(59) Glerup, J.; Weihe, H. *Acta Chem. Scand.* **1991**, *45*, 444−448.
(60) Glerup, J.; Weihe, H. *Inorg. Chem.* **1997**, *36*, 2816−2819.
(61) Abragam, A.; Bleaney, B. *Electron Paramagnetic Resonance of Transition Ions*; Dover: New York, 1970.

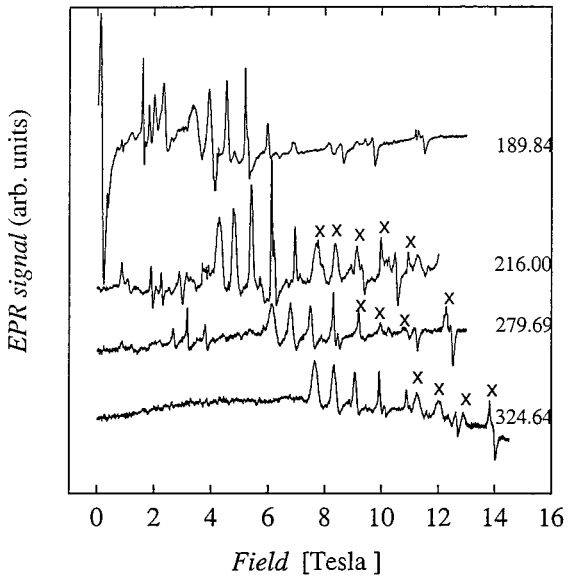

Figure 2. High-frequency EPR spectra for a sample of $[Fe_2(\mu\text{-}OH)_3(tmtacn)_2]^{2+}$ pressed in a KBr pellet collected at 20 K over the 189−324 GHz nominal frequency range. Each spectrum is labeled with its nominal frequency. Features marked with an "x" arise from a higher harmonic of the fundamental frequency, as indicated in Table 1.

the ZFS is likely dominated by D, with a small E possible from the reduced site symmetry.

An initial interpretation of the sets of fine structure visible in the spectra shown in Figure 2 is that they are either parallel or perpendicular resonances between the various Kramers doublets, of which only a few are thermally populated at 20 K. In the strong-field limit with $E = 0$, the spacing between interdoublet lines should be regular and follow eq 4, where θ is the angle between the external magnetic field and the principal magnetic axis of the $S = {}^9/_2$ cation. This leads to spacing between perpendicular resonances of $D/(2g_\perp\beta)$, whereas the spacing between parallel resonances is $D/(g_{//}\beta)$. Thus, if $g_\perp \simeq g_{//}$, the spacings between lines in fine structure for a parallel transition would be twice those for a perpendicular transition.

$$H_r = g_e/g[h\nu/g_e\beta + (2M_s + 1)D'/2] \qquad (4)$$

where $D' = (3\cos\theta - 1)D/g_e\beta$.

Two distinct sets of fine structure are seen for complex **1**, one at low-field and one at high-field, as shown in Figure 2. The low-field set of five lines moves to higher resonance field as the microwave frequency is increased, that is, from the 3.5−6 T range at 189.84 GHz, to the 7.7−11 T range at 324.64 GHz. The higher-field set of 2−3 lines appears to also move to higher field as frequency is increased, from the 9−12 T range at 189.84 GHz, to the 13−14 T range at 324.64 GHz. In addition, several other lines can be seen in the 0−2 T range at 189.84 GHz. In each of the data sets collected over the nominal frequency range 216−325 GHz, an "extra" set of fine structure appears (marked by an "x") which arises from a higher harmonic of the Gunn diode. For example, the resonances from 432.85 GHz (fourth harmonic of 108.21 GHz) are apparent in the data set collected at a nominal frequency of 324.64 GHz (third harmonic of 108.21 GHz), as described in the Experimental Section.

The spacing between the group of lower field lines is smaller than the spacing between the group of higher field lines, implying that the fine structure at lower field is likely due to the perpendicular resonances (eq 4). The resonant field positions for these perpendicular transitions are listed in Table 1. A preliminary estimate of $D/g_\perp$ can then be made from the splitting between the two lowest field lines at 324.64 GHz, which leads to $|D|/g_\perp = 0.3$, or $|D| = 0.6$ cm^{-1} for $g_\perp = 2$. However, the spacing between these lines at a given frequency is not regular, even at 324.64 GHz, indicating that either the strong-field limit has not been reached, or that higher order ZFS terms are relevant. It was necessary to simulate the spectra to determine g and D using these preliminary values.

Table 1. Perpendicular HFEPR Transition Fields for $[Fe_2(\mu\text{-}OH)_3(tmtacn)_2]^{2+}$ at 20 K Over the 189−440 GHz Frequency Range

	transition field (tesla)					
transition $M_s \rightarrow M_s + 1$	189.84 GHz	216.00 GHz	279.69 GHz	324.64 GHz	372.92 GHz[a]	432.85 GHz[b]
$^{-9}/_2 \rightarrow {}^{-7}/_2$	3.52	4.38	6.28	7.76	9.27	11.38
$^{-7}/_2 \rightarrow {}^{-5}/_2$	4.01	4.87	6.88	8.43	9.98	12.15
$^{-5}/_2 \rightarrow {}^{-3}/_2$	4.58	5.46	7.58	9.15	10.94	12.97
$^{-3}/_2 \rightarrow {}^{-1}/_2$	5.21	6.13	8.35	9.98	NA[c]	13.91
$^{-1}/_2 \rightarrow {}^{+1}/_2$	5.99	6.95	9.27	10.92	NA[c]	NA[c]

[a] Observed as a higher harmonic in the 279.69 GHz spectrum. [b] Observed as a higher harmonic in the 324.64 GHz spectrum. [c] Not apparent.

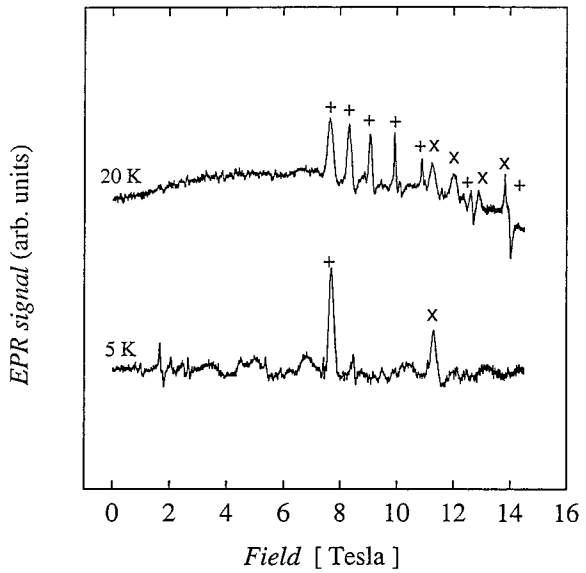

Figure 3. HFEPR spectra for a sample of $[Fe_2(\mu\text{-}OH)_3(tmtacn)_2]^{2+}$ pressed in a KBr pellet collected at 5 and 20 K at a nominal frequency of 324.6 GHz. Features marked with a "+" arise from 324.6 GHz (third harmonic of 108.2 GHz), whereas features marked with a "x" arise from 432.8 GHz (fourth harmonic of 108.2 GHz).

A representative spectrum was collected at lower temperature in order to experimentally confirm the sign of D. As shown in Figure 3, at 5 K only the lowest field line has appreciable intensity for both the 324.65 and 432.85 GHz frequencies which are present as the third and fourth harmonics, respectively, of the 110 GHz Gunn diode. The intensities of EPR transitions reflect the Boltzmann population differences between the energy levels, and therefore indicate which M_s levels lie at lowest energies. Inspection of an energy vs magnetic field diagram (Figure 4) generated using a positive D value ($D = +1.1$ cm^{-1}) shows the energies of the M_s levels and the spacing of parallel and perpendicular resonant fields. The lowest energy doublet for a positive D value is the $\pm{}^1/_2$ doublet; the other Kramers doublets lie higher in energy by (DM_s^2) cm^{-1}. A magnetic field breaks the Kramers degeneracies, leading to the illustrated energy splittings. In the upper part of Figure 4 is shown how a magnetic field oriented in a parallel fashion (i.e., along the magnetic z axis) splits the five Kramers doublets. The energy

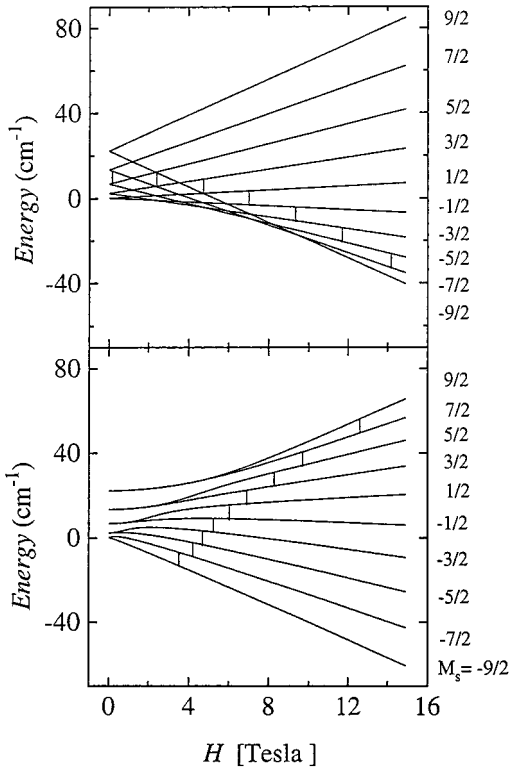

Figure 4. Energy vs Field of the 10 energy levels deriving from an $S = {}^9/_2$ spin state having $g = 2$ that is split by an axial zero-field splitting $D = +1.1$ cm^{-1}. The field, H, is parallel (top) or perpendicular (bottom) to the molecular magnetic *z* axis. The energy levels are labeled according to their dominant parentage at high magnetic fields. The vertical bars represent selected resonant field positions at 189.84 GHz (6.33 cm^{-1}).

of each component varies linearly with the magnetic field. At very low fields, the $M_s = -{}^1/_2$ level is the ground state. Finally, at fields above ca. 9 T the $M_s = -{}^9/_2$ level becomes the ground state.

In the lower part of Figure 4 the energies of the various levels are plotted as a function of the external magnetic field oriented perpendicularly. In this case the magnetic field causes appreciable mixing of the M_s levels. Due to this mixing, the two components of the zero-field $\pm{}^1/_2$ Kramers doublet immediately split and become the $M_s = -{}^9/_2$ and $-{}^7/_2$ levels. At high enough temperatures there would be appreciable Boltzmann populations in all components of the $S = {}^9/_2$ ground state. In this case, vertical lines are drawn to show all of the parallel and prependicular transitions that would be seen at 189.84 GHz. Clearly, at temperatures very low relative to the ZFS, a single resonance at the lowest resonant field of the perpendicular fine structure would be observed, for all molecules would populate the lowest energy M_s level, the $M_s = -{}^9/_2$ level. As shown in the lower part of Figure 4, a single transition at ca. 3.6 T would be seen for the perpendicular signal. Conversely, for *D* negative a resonance at the highest resonant field of the perpendicular fine structure would be observed at very low temperatures. This is contrasted with the situation for the parallel resonances, in which the opposite trend would be observed.[40] Our observation of a single resonance at 5 K at the lowest resonant field of the perpendicular fine structure confirms that *D* is positive. Also, the observation of only one significantly intense transition indicates that the ZFS is the same order of magnitude as thermal energy at 5 K, which is consistent not only with our initial estimate of *D*, but also with prior estimates from Mössbauer[20] and magnetic susceptibility[23] experiments.

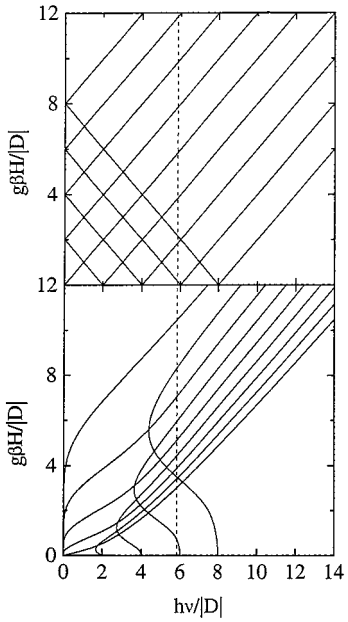

Figure 5. Plot of Zeeman energy vs. microwave energy, normalized by *D*, for an $S = {}^9/_2$ spin. The plotted lines indicate the resonant field position (H) as a function of the microwave frequency, ν, for high-field transitions which are $\Delta M_s = 1$. The applied magnetic field is parallel (top) or perpendicular (bottom) to the molecular *z*-axis. The dashed vertical line corresponds to $\nu = 189.84$GHz, $D = +1.08$ cm^{-1}.

Simulations. Although the above analysis of the experimental spectra yielded a set of g and ZFS parameters that were fairly well confirmed by preliminary simulations of the spectra, some meaningful constraints were necessary to improve the agreement between the simulations and experiment. Resonant field vs frequency plots (Figure 5) were constructed to better understand the observed resonances. In these diagrams, the resonant field is plotted as a function of the microwave energy, each of which is normalized by the value of *D*. For a given value of $h\nu/|D|$, one may draw a vertical line which will cross the calculated resonant field positions for the parallel (upper diagram) and perpendicular (lower diagram) transitions. Inspection revealed that a transition near zero-field, such as is observed in the 189.84 GHz spectrum, will occur only for simple multiples of $h\nu/|D|$. The energy of the 189.84 GHz radiation is 6.33 cm^{-1}, which led us to focus on the region near $h\nu/D = 6$, suggesting that this near-zero field resonance is likely that between the $M_s = +{}^7/_2$ and $+{}^5/_2$ levels. This resonance is very intense since the parallel and perpendicular components virtually overlap. The value of *D* was determined by this resonance field using eq 5.

$$-g\beta H_r + 6D = \Delta E = h\nu \qquad (5)$$

It was noted that this resonance would not be very sensitive to *g*, and therefore would provide an estimate of *D* independent of the *D*/*g* ratio. For $h\nu = 6.33$ cm^{-1} and $H_r = 0.14$ T, the value of *D* was calculated to be $+1.078(1)$ cm^{-1} for g in the range of 2.00−2.20; therefore *D* was constrained to $+1.08$ cm^{-1} in the final simulations. The final parameters which were used for the plotted simulations are $g_{iso} = 2.00$, $D = +1.08$ cm^{-1}, and $E = 0$ cm^{-1}. Representative simulations at 189.84 (Figure 6), 324.64, and 432.85 GHz (Figure 7) are plotted with the corresponding experimental spectra. Very good agreement was found between the simulations and the experimental spectra using this set of parameters. Reasonable simulations were also found at lower frequencies with $g_\perp = 1.985$; however, it was not possible to change $g_{//}$ appreciably from 2.00 with $D = +1.08$

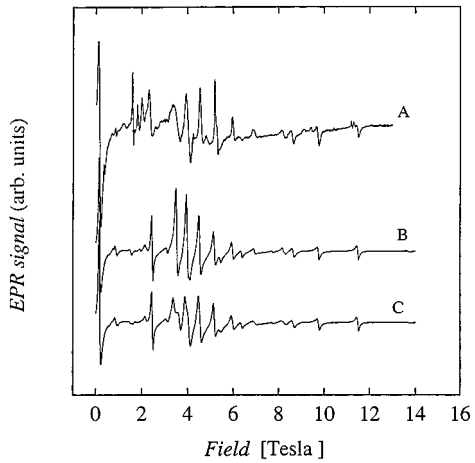

Figure 6. (A) HFEPR spectra for a sample of $[Fe_2(\mu\text{-}OH)_3(tmtacn)_2]^{2+}$ pressed in a KBr pellet collected at 20 K at a frequency of 189.84 GHz. (B) Simulated 189.84 GHz HFEPR spectrum using the following parameters: $g_x = g_y = g_z = 2.00$, $D = +1.08$ cm^{-1}. (C) Simulated 189.84 GHz HFEPR spectrum using the following parameters: $g_x = g_y = g_z = 2.00$, $D = +1.08$ cm^{-1}, $E = +0.01$ cm^{-1}.

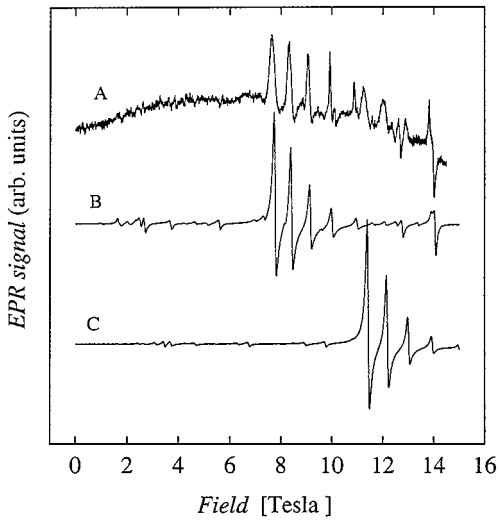

Figure 7. (A) HFEPR spectra for a sample of $[Fe_2(\mu\text{-}OH)_3(tmtacn)_2]^{2+}$ pressed in a KBr pellet collected at 20 K at a nominal frequency of 324.64 GHz. (B) Simulated 324.64 GHz HFEPR spectrum using the following parameters: $g_x = g_y = g_z = 2.00$, $D = +1.08$ cm^{-1}. (C) Simulated 432.85 GHz HFEPR spectrum using the following parameters: $g_x = g_y = g_z = 2.00$, $D = +1.08$ cm^{-1}.

cm^{-1} and still reproduce the experimental spectra. Tables2−5 contain the observed and simulated resonant fields for all frequencies; the agreement is very good with respect to both resonant field positions and fine structure spacings.

Two comments about the simulations of the 189.84 GHz spectrum are in order (see Figure 6 and Table 2). The transitions observed in the 1.6−2.1 T range are not artifacts from the fundamental frequency but are likely off-axis turning points. Second, it is difficult in running a HFEPR spectrum to obtain a purely first-derivative spectrum. The simulated spectrum is calculated as purely derivative spectrum, thus there are differences seen in the line shapes between experimental and simulated spectra.

The angular variation in resonant field position of the dominant interdoublet resonances at 189.84 GHz is shown in Figure 8. The low-field region (0−4 T) is plotted separately in Figure 9. Since there is extensive level crossing in this region, only those transitions that give rise to appreciable EPR intensity

Table 2. HFEPR Transition Fields for a Powdered Sample of $[Fe_2(\mu\text{-}OH)_3(tmtacn)_2]^{2+}$ 189.84 GHz and 20 K

	transition field (tesla)		
transition[a]	observed	calculated	
$M_s \rightarrow M_s + 1$	189.84 GHz	(sim I)[b]	(sim II)[c]
$+5/2 \rightarrow +7/2$	0.14	0.18	0.18
	1.61	1.54	1.53
	1.83	1.96	1.94
	2.03	2.17	2.20
$+3/2 \rightarrow +5/2$ //	2.35	2.46	2.46
$-9/2 \rightarrow -7/2$ ⊥	3.52	3.56	3.53
$-7/2 \rightarrow -5/2$ ⊥	4.01	4.02	3.99
$-5/2 \rightarrow -3/2$ ⊥	4.58	4.57	4.53
$-3/2 \rightarrow -1/2$ ⊥	5.21	5.22	5.18
$-1/2 \rightarrow +1/2$ ⊥	5.99	6.02	5.97
$+1/2 \rightarrow +3/2$ ⊥	6.92	6.98	6.93
$+3/2 \rightarrow +5/2$ ⊥	8.21	8.27	8.21
$-1/2 \rightarrow +1/2$ TP	8.59	8.67	8.65
$-3/2 \rightarrow -1/2$ TP	9.70	9.76	9.76
$-5/2 \rightarrow -3/2$ TP	11.44	11.48	11.48

[a] Transitions were assigned by simulations. The parallel edges are denoted by "//", the perpendicular edges are denoted "⊥", and the turning points are denoted "TP." [b] Simulation using the following parameters: $g_x = g_y = 1.985$, $g_z = 2.00$, $D = +1.08$ cm^{-1}. [c] Simulation using the following parameters: $g_x = g_y = g_z = 2.00$, $D = +1.08$ cm^{-1}.

Table 3. HFEPR Transition Fields for a Powdered Sample of $[Fe_2(\mu\text{-}OH)_3(tmtacn)_2]^{2+}$ at 216.00 GHz and 20 K

	transition field (tesla)		
transition[a]	observed	calculated	
$M_s \rightarrow M_s + 1$	216.00 GHz	(sim I)[b]	(sim II)[c]
$-9/2 \rightarrow -7/2$ ⊥	4.38	4.35	4.30
$-7/2 \rightarrow -5/2$ ⊥	4.87	4.85	4.81
$-5/2 \rightarrow -3/2$ ⊥	5.46	5.45	5.40
$-3/2 \rightarrow -1/2$ ⊥	6.13	6.15	6.10
$-1/2 \rightarrow +1/2$ ⊥	6.95	6.99	6.94
325[d]	7.77		
$+1/2 \rightarrow +3/2$ ⊥	7.97	8.02	7.95
325[d]	8.46		
325[d]	9.18		
	9.35	9.42	9.40
325[d]	10.00		
$-3/2 \rightarrow -1/2$ TP	10.50	10.55	10.55
325[d]	10.94		
	11.37		
$-5/2 \rightarrow -3/2$ TP		12.36	12.36

[a] Transitions were assigned by simulation. The turning point (TP) and perpendicular (⊥) resonances descriptions were made by analogy with the 190 GHz spectrum. [b] Simulation using the following parameters: $g_x = g_y = 1.985$, $g_z = 2.00$, $D = +1.08$ cm^{-1}. [c] Simulation using the following parameters: $g_x = g_y = g_z = 2.00$, $D = +1.08$ cm^{-1}. [d] These features arise from the 325 GHz frequency that is present as the third harmonic.

are plotted. In these diagrams, β is the angle between the external magnetic field and the molecular magnetic z axis; $\beta = 0°$ corresponds to H_{ext} being parallel to z (e.g., the parallel edge), whereas $\beta = 90°$ corresponds to H_{ext} being perpendicular to z (e.g., the perpendicular edge). The curves in Figure 8 progress from the $+3/2 \rightarrow +5/2$ transition (curve A) on through to the $-9/2 \rightarrow -7/2$ transition (curve G) for each of the high-field interdoublet transitions. A feature will be apparent in the EPR spectrum from field extrema in the angular variation of a resonance, which frequently are only observed at the parallel and perpendicular edges. Due to the large ZFS, a great deal of level mixing occurs and turning points are prominent in all of the curves; in particular, the fine structure observed at higher fields is due to these turning points rather than to the parallel

Table 4. HFEPR Transition Fields for a Powdered Sample of $[Fe_2(\mu\text{-}OH)_3(tmtacn)_2]^{2+}$ at 279.69 GHz and 20 K

transition[a] $M_s \rightarrow M_s + 1$	transition field (tesla) observed 279.69 GHz	calculated (sim I)[b]	calculated (sim II)[c]
$-9/2 \rightarrow -7/2\ \perp$	6.28	6.35	6.30
$-7/2 \rightarrow -5/2\ \perp$	6.88	6.96	6.91
$-5/2 \rightarrow -3/2\ \perp$	7.58	7.66	7.59
$-3/2 \rightarrow -1/2\ \perp$	8.35	8.46	8.39
	8.52		
$-1/2 \rightarrow +1/2\ \perp$, and 373[d]	9.27	9.39	9.31
373[d]	9.98		
	10.34	10.48	10.41
373[d]	10.94		
	11.24	11.37	11.34
	12.30	12.29	12.29
	12.50	12.57	12.56

[a] Transitions were assigned by simulation. [b] Simulation using the parameters: $g_x = g_y = 1.985$, $g_z = 2.00$, $D = +1.08\ cm^{-1}$. [c] Simulation using the parameters: $g_x = g_y = g_z = 2.00$, $D = +1.08\ cm^{-1}$. [d] These features arise from the fourth harmonic (373 GHz) and were identified by simulation.

Table 5. HFEPR Transition Fields for a Powdered Sample of $[Fe_2(\mu\text{-}OH)_3(tmtacn)_2]^{2+}$ at 324.65 GHz and 20 K

transition[a] $M_s \rightarrow M_s + 1$	transition field (tesla) observed 324.65 GHz	calculated (sim I)[b]	calculated (sim II)[c]
$-9/2 \rightarrow -7/2\ \perp$	7.76	7.83	7.78
$-7/2 \rightarrow -5/2\ \perp$	8.43	8.50	8.44
$-5/2 \rightarrow -3/2\ \perp$	9.15	9.25	9.18
$-3/2 \rightarrow -1/2\ \perp$	9.98	10.10	10.03
	10.16		
	10.92	11.08	10.99
	11.36	11.58	
$-9/2 \rightarrow -7/2\ \perp$[d]	11.38	11.51	11.43
$-7/2 \rightarrow -5/2\ \perp$[d]	12.15	12.29	12.19
	12.46	12.62	12.56
	12.68	12.81	12.78
$-5/2 \rightarrow -3/2\ \perp$[d]	12.97	13.13	13.02
$-3/2 \rightarrow -1/2\ \perp$[d]	13.91	14.05	13.95
	14.00	14.06	14.06

[a] Transitions were assigned by simulation. [b] Simulation using the following parameters: $g_x = g_y = 1.985$, $g_z = 2.00$, $D = +1.08\ cm^{-1}$. [c] Simulation using the following parameters: $g_x = g_y = g_z = 2.00$, $D = +1.08\ cm^{-1}$. [d] Features from the fourth harmonic of 108.21 GHz (432.85) were evident in the experimental spectrum and were simulated with the same set of parameters as the 324.65 GHz spectra.

edges of the interdoublet resonances. The resonant field position of these turning points is not obvious from simple considerations, and they are therefore difficult to interpret with regard to the *D* and *g* values. In contrast, the resonant field of the parallel edges may be simply calculated from eq 4, and then related to *g* and *D*. In the presence of a turning point, the parallel resonance is very weak, and therefore difficult to observe in a powder spectrum. For this reason, the expected signature resonance between the $M_s = -1/2$ and $+1/2$ energy levels (curve *D*, Figure 8) is not observed at the parallel edge, preventing a direct measurement of $g_{//}$. Also, the turning points do not follow a regular spacing, making spectral simulation the only way to evaluate the spin-Hamiltonian parameters.

With simulations, we were better able to understand the decrease in line width with increasing field throughout the low-field fine structure, as shown in Figure 2. For example, at 189.84 GHz there is an obvious decrease in line width when one moves from the line at 3.52 T to the line at 5.21 T; this is the progression from a $-9/2 \rightarrow -7/2$ transition to the $-3/2 \rightarrow -1/2$ transition. Quantifying experimental line widths is difficult, due to line shape uncertainty, but this trend is nevertheless obvious at all frequencies. It is noted that a small rhombic ZFS would lead to a splitting of the perpendicular resonances, with larger splittings for larger M_s values, which might lead to anisotropic broadening as observed here; perhaps this is the origin of some of the line width variation.

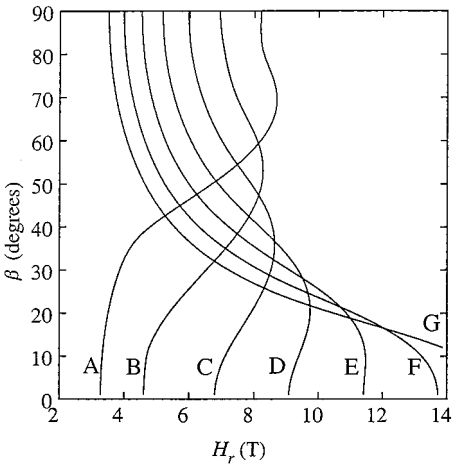

Figure 8. Resonant field vs angle for selected allowed HFEPR transitions at 189.84 GHz for $g = 2$, $D = +1.08\ cm^{-1}$. The angle β measures the angle between the external magnetic field and the molecular *z* axis. The indicated transitions occur between energy levels that are labeled according to their dominant parentage at high field. (A) $+3/2 \rightarrow +5/2$; (B) $+1/2 \rightarrow +3/2$; (C) $-1/2 \rightarrow +1/2$; (D) $-3/2 \rightarrow -1/2$; (E) $-5/2 \rightarrow -3/2$; (F) $-7/2 \rightarrow -5/2$; (G) $-9/2 \rightarrow -7/2$.

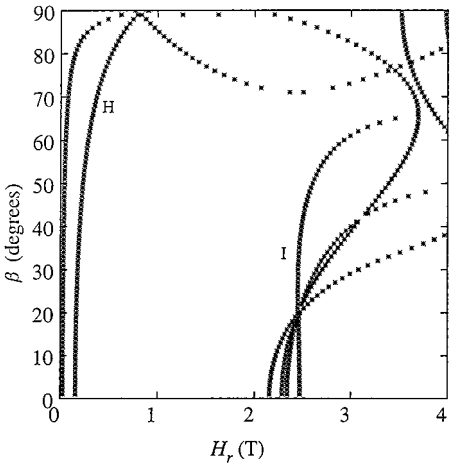

Figure 9. Resonant field vs angle for selected allowed HFEPR transitions at 189.84 GHz for $g = 2$, $D = +1.08\ cm^{-1}$. The angle β measures the angle between the external magnetic field and the molecular *z* axis. The indicated transitions occur between energy levels that are labeled according to their dominant parentage at low field. Many transitions are not labeled, as their parentage is uncertain or very complicated from field-induced admixture of spin-states. (H) $+5/2 \rightarrow +7/2$; (I) $-7/2 \rightarrow -9/2$ and $+3/2 \rightarrow +5/2$.

An inspection of the observed and simulated resonant fields reveals that the simulations predict a slightly reduced spacing between the perpendicular resonances than is observed, which could indicate that the $D/g_\perp$ ratio used in the simulations is too small; however, the presence of a small rhombic ZFS would lead to subtle changes in the apparent perpendicular splittings, and cannot be discounted. Since *D* was constrained to + 1.08-(1) cm^{-1} by eq 4, we tried to decrease $g_\perp$, but this resulted in simulations which were less satisfactory at higher frequencies.

In the face of this, and the increased line widths for transitions originating from larger M_s levels, it is almost certain that a small E is present for the $S = {}^9/_2$ ground state of complex **1**. A trial simulation at 189.84 GHz using $g_{iso} = 2.00$, $D = +1.08$ cm^{-1}, and $E = 0.01$ cm^{-1} is shown in Figure 6C. Clearly, a nonuniform line width is produced, as is an altered spacing between the perpendicular resonances. It is noted that we could have performed simulations in which this small E was used, with a consequent increase in the D/g ratio, but this complicated the analysis. A simulation incorporating a small anisotropy in $g_\perp$ ($g_z = 2.00$, $g_x = 2.02$, $g_y = 1.98$) led to approximately uniform broadening of all perpendicular resonances, and consequently anisotropy in $g_\perp$ could not account for the observed line width variations. Clearly, a small E value is present. Since very good simulations were obtained with a simple set of parameters, we consider that the electronic structure of complex **1** is adequately described by $g_x = g_y = g_z = 2.00(2)$, $D = +1.08(1)$ cm^{-1}, and $E = 0.00(1)$ cm^{-1}, with possible contributions from higher order ZFS terms being negligibly small.

Concluding Comments

High-frequency EPR has been successfully applied to the electronically delocalized mixed-valence dinuclear complex $[Fe_2(OH)_3(tmtacn)_2]^{2+}$, and spin-Hamiltonian parameters have been determined by spectral simulation of the HFEPR powder patterns. The spin-Hamiltonian parameters from HFEPR spectra were determined by direct observation of resonance between the various M_s levels of the ground $S = {}^9/_2$ state, providing the most sensitive measurements for these parameters. It was found that the zero-field splitting is positive ($M_s = \pm{}^1/_2$ doublet at the lowest energy) and essentially axial, as characterized by the following parameters: $D = +1.08(1)$ cm^{-1} and $E < 0.01$ cm^{-1}. The currently determined value of D is somewhat smaller than prior reports suggested.[20,23] However, the D value evaluated in this HFEPR work is well determined by the observation of a low-field transition between the $+{}^5/_2$ and $+{}^7/_2$ levels. The **g** tensor was determined to be essentially isotropic with $g_x \simeq g_y \simeq g_z \simeq 2.00(2)$, at variance with the prior results which suggested a highly anisotropic **g** tensor with $g_{//} = 2.3$ and $g_\perp = 2.04$. It is noted that the prior estimate of **g** was obtained by X-band EPR, in which the only transitions observed were the perpendicular and parallel components of the $M_s = -{}^1/_2$ to $+{}^1/_2$ transition, both of which were very broad.

The current work demonstrates the utility of HFEPR for the study of high-spin dinuclear iron compounds, such as those found in many proteins. Resonances between the various Kramers doublets provide a direct spectroscopic measurement of the zero-field splitting parameters. In principle, the components of the **g** tensor may be obtained by variable frequency measurements, however this work and recent work[50] on other high-spin molecules suggests that HFEPR on powders is not very discriminating to small anisotropies in **g**, due to a combination of large line widths and to line shape uncertainty.

Acknowledgment. We thank Dr. Joe Goldsby of Florida State University for the use of a KBr press. We are particularly thankful to Dr. Høgni Weihe who not only gave us a copy of the EPR simulation program but also worked to make it compatible with a 400 MHz computer. J.K. and L.C.B. thank the NHFML for support. D.N.H. acknowledges the NSF for funding. M.J.K. thanks the NIH for support from the Heme training grant (2 T32-DK07233) and the NHFML visitor's program for partial funding of this research.

Supporting Information Available: Hamiltonian energy matrix elements for the three different magnetic field directions. This material is available free of charge via the Internet at http://pubs.acs.org.

IC9901012